Development and characterization of CD54-targeted immunoPET imaging in solid tumors

Weijun Wei[1,2], **Dawei Jiang**[2], **Hye Jin Lee**[3], **Miao Li**[2,4], **Christopher J. Kutyreff**[2], **Jonathan W. Engle**[2], **Jianjun Liu**[1], **Weibo Cai**[2,3,5]

[1]Department of Nuclear Medicine, Renji Hospital, School of Medicine, Shanghai Jiao Tong University, 1630 Dongfang Rd, Shanghai 200127, China

[2]Departments of Radiology and Medical Physics, University of Wisconsin - Madison, Room 7137, 1111 Highland Avenue, Madison, WI 53705-2275, USA

[3]School of Pharmacy, University of Wisconsin - Madison, Room 7137, 1111 Highland Avenue, Madison, WI 53705-2275, USA

[4]Department of Radiology, The First Affiliated Hospital of Xi'an Jiaotong University, 277 West Yanta Rd, Xi'an 710061, Shanxi, China

[5]University of Wisconsin Carbone Cancer Center, Madison, WI 53705, USA

Abstract

Purpose—Intercellular adhesion molecule-1 (ICAM-1, CD54) is an emerging therapeutic target for a variety of solid tumors including melanoma and anaplastic thyroid cancer (ATC). This study aims to develop an ICAM-1-targeted immuno-positron emission tomography (immunoPET) imaging strategy and assess its diagnostic value in melanoma and ATC models.

Methods—Flow cytometry was used to screen ICAM-1-positive melanoma and ATC cell lines. Melanoma and ATC models were established using A375 cell line and THJ-16T cell line, respectively. An ICAM-1-specific monoclonal antibody (R6–5-D6) and a nonspecific human IgG were radiolabeled with ^{64}Cu and the diagnostic efficacies were interrogated in tumor-bearing mouse models. Biodistribution and fluorescent imaging studies were performed to confirm the specificity of the ICAM-1-targeted imaging probes.

Results—ICAM-1 was strongly expressed on melanoma and advanced thyroid cancer cell lines. ^{64}Cu-NOTA-ICAM-1 immunoPET imaging efficiently delineated A375 melanomas with a peak tumor uptake of 21.28 ± 6.56 %ID/g ($n = 5$), significantly higher than that of ^{64}Cu-NOTA-IgG (10.63 ± 2.58 %ID/g, $n = 3$). Moreover, immunoPET imaging with ^{64}Cu-NOTA-ICAM-1 efficiently visualized subcutaneous and orthotopic ATCs with high clarity and contrast.

Fluorescent imaging with IRDye 800CW-ICAM-1 also visualized orthotopic ATCs and the tumor uptake could be blocked by the ICAM-1 parental antibody R6–5-D6, indicating the high specificity of the developed probe. Finally, blocking with the human IgG prolonged the circulation of the ^{64}Cu-NOTA-ICAM-1 in R2G2 mice without compromising the tumor uptake.

Conclusion—ICAM-1-targeted immunoPET imaging could characterize ICAM-1 expression in melanoma and ATC, which holds promise for optimizing ICAM-1-targeted therapies in the future.

Keywords

ICAM-1; ImmunoPET; Companion diagnostics; Thyroid cancer; Melanoma

Introduction

Intercellular adhesion molecule-1 (ICAM-1, CD54), a member of the immunoglobulin superfamily of adhesion molecules, is composed of five extracellular immunoglobulin G-like domains and a short cytoplasmic tail [1]. ICAM-1 and vascular cell adhesion molecule-1 (VCAM-1) are well-characterized markers for inflammation [2]. While ICAM-1 expression is very low or absent in normal organs (e.g., liver, pancreas, thyroid, ovary, breast, prostate, heart, and skin), it is highly expressed on the surface of many types of cancer cells [1, 3]. The upregulation of ICAM-1 is required to initiate the transmigration and spread of melanomas [4–6]. ICAM-1 is also aberrantly expressed in thyroid cancers [7]. Interestingly, ICAM-1-targeted chimeric antigen receptor T (CAR-T) cells showed robust killing of thyroid cancer cells in vitro. More importantly, the administration of ICAM-1 CAR-T cells demonstrated profound and enduring tumor eradication in preclinical anaplastic thyroid cancer (ATC) xenograft models [8, 9]. The evidence provides a rationale for utilizing ICAM-1 as a target for diagnosing and treating aggressive melanomas and thyroid cancers.

Traditional tumor maker screening techniques, such as immunohistochemistry, can only examine resected tumors and local lymph nodes. In comparison, molecular imaging approaches could noninvasively detect and quantify tumor markers or receptor status across the body when multiple metastases have developed. Several molecular imaging modalities are being used [10], including magnetic resonance (MR) imaging, single-photon emission computed tomography (SPECT), and positron emission tomography (PET). After conjugating an anti-ICAM-1 antibody to iron oxide nanoparticles (IONPs), a study reported that MR imaging using ICAM-IONPs could quantify ICAM-1 overexpression in breast cancer models [11]. When it comes to analyzing receptor concentrations or tumor markers in cancers, PET is more commonly used than SPECT and MRI because of its inherent advantages (i.e., quantitation and resolution). In recent years, immunoPET, a companion diagnostic method developed by conjugating a therapeutic antibody to a positron emitter, is being increasingly developed and used in clinical settings [12]. In addition to its role in imaging receptor tyrosine kinases and oncoproteins in cancers [12–16], immunoPET allows noninvasive evaluation of the dynamics of immune cells [17], as a result, optimizing or even changing clinical treatment decisions. Moreover, immunoPET could facilitate antibody drug development by providing the in vivo biodistribution and pharmacokinetics of therapeutic antibodies [18].

Despite the emerging role of ICAM-1 as a therapeutic target for a wealth of malignancies, molecular imaging toolbox specific for ICAM-1 is still missing. In this study, we aim to develop an ICAM-1 targeting immunoPET probe ^{64}Cu-NOTA-ICAM-1 and investigate its diagnostic performance in preclinical melanoma and ATC models.

Materials and methods

Cell lines and flow cytometry

Two melanoma cell lines (SK-MEL-5 and A375) were kindly provided by Dr. Mark R. Albertini (University of Wisconsin - Madison) and cultured in phenol red-free Dulbecco's Modified Eagle's Medium (DMEM, ATCC) supplemented with 10% fetal bovine serum (FBS, Gibco). Five thyroid cancer cell lines (THJ-16T, 8505C, TPC-1, FTC-236, and FTC-133) were kindly provided by Dr. Heather Hardin (University of Wisconsin - Madison). THJ-16T[Luc] cell line was constructed by transfecting the THJ-16Tcell line with a pGMLV-CMV-Lu lentivirus luciferase reporter (Genomeditech). Thus, the tumor burden of mice bearing orthotopic ATCs can be monitored by bioluminescence imaging (BLI). All the thyroid cancer cell lines were maintained according to the recommended cell culture protocols.

For detecting cell surface abundance of ICAM-1 by flow cytometry, a mouse anti-human ICAM-1 monoclonal antibody (mAb) (Clone: R6–5-D6; BioXCell) was used. Concretely speaking, 1×10^6 cells for each sample were collected and washed with cold phosphate-buffered saline (PBS, HyClone). The washed cells were re-suspended in flow cytometry staining buffer (Invitrogen) and incubated with primary antibodies (5 μg/mL or 10 μg/mL of NOTA-ICAM-1) on ice for 45 min, followed by washing with PBS for three times. The washed cells were further incubated with an Alexa Fluor 488-labeled goat anti-mouse IgG (5 μg/mL) for another 45 min. The samples were washed again, re-suspended in PBS, and analyzed using a BD LSR Fortessa flow cytometer (BD Biosciences). The results were analyzed with the FlowJo software (FlowJo LLC).

Melanoma and thyroid cancer models

All animal experiments were conducted in compliance with the institutional guidelines at the University of Wisconsin - Madison and at the Renji Hospital, School of Medicine, Shanghai Jiao Tong University. A375 cells suspended in sterile PBS and matrigel matrix (Corning) with a ratio of 1:1 were used to establish subcutaneous melanoma models [19]. We have reported that the ATC cell line THJ-16T has a tumor take rate as high as 100% in athymic nude mice [20], and orthotopic thyroid cancer models better mirror the aggressive scenario of advanced thyroid cancers [21, 22]. Therefore, we chose the THJ-16T cell line and the ultra-immunodeficient R2G2 (B6;129-Rag2[tm1Fwa]IL2rg[tm1Rsky]/DwlHsd; Envigo) mice to establish thyroid cancer models. Following a previously described protocol [20], 5×10^6 THJ-16T cells and $0.5–1 \times 10^6$ THJ-16T cells per mouse were used to establish subcutaneous and orthotopic ATC xenografts, respectively. To facilitate BLI, orthotopic ATC models were also established using the THJ-16T[Luc] cell line and nude mice. The ATC models were used for immunoPET and fluorescent imaging 4–5 weeks after tumor cell inoculation.

Radiolabeling, immunoPET imaging, and data analysis

The ICAM-1-specific mAb R6–5-D6 and a nonspecific human IgG isotype control (Invitrogen) were used to conjugate immunoPET probes in this study. Antibodies were first conjugated with 2-S-(4-Isothiocyanatobenzyl)-1,4,7-triazacyclononane-1,4,7-triacetic acid (p-SCN-Bn-NOTA; Macrocyclics) and then radiolabeled with ^{64}Cu ($T_{1/2}$ = 12.7 h) [23]. Briefly, the storage buffer of antibodies was changed to PBS and the pH of the antibody solution was adjusted to 9.0–10.0 using 0.1 M Na_2CO_3. The chelator NOTA was dissolved in dimethyl sulfoxide and added to the antibody solution with a molar ratio of 10:1, followed by incubation of the mixture on a shaker (800 rpm) at room temperature for 2 h. NOTA-conjugated antibodies were purified with equilibrated PD-10 desalting columns (GE Healthcare) and concentrated with Amicon® Ultra-4 Centrifugal Filters (with a molecular weight cut-off of 100 KDa; Millipore). The conjugated antibodies were used immediately or stored at − 20 °C for subsequent use. For radiolabeling, ^{64}Cu of high specific activity was produced in house and 3–5 mCi of ^{64}Cu in 0.1 HCl was added to 300 μL of NaOAc (pH 5 ± 0.5), followed by addition of 100–200 μg of NOTA-mAb to the radiometal solution and incubation at 37 °C for 1 h under constant shaking. The final radiopharmaceuticals were separated from free ^{64}Cu using PD-10 columns with PBS as the mobile phase.

The radiochemical purity (RCP) of the radiopharmaceuticals was assessed by radio-thin layer chromatography (radio-TLC). Moreover, ^{64}Cu-NOTA-ICAM-1 was incubated in 1× PBS buffer and 100% mouse serum for 48 h and the stability was tested by performing radio-TLC and then measured by a gamma counter (Perkin Elmer Inc.). On average, 10.25 ± 1.96 MBq of ^{64}Cu-NOTA-ICAM-1 (n = 14) and 9.52 ± 2.49 MBq of ^{64}Cu-NOTA-IgG (n = 6) were injected via tail vein to the experimental mice, as specified below. For blocking studies, 1.5 mg of human IgG isotype control per mouse was injected one day prior to ^{64}Cu-NOTA-ICAM-1 immunoPET imaging. ImmunoPET imaging was acquired sequentially using an Inveon PET/CT scanner (Siemens) and the data were analyzed as previously described [19].

Bioluminescent and fluorescent imaging studies

IRDye 800CW-ICAM-1 was developed by labeling the mAb R6–5-D6 with a near-infrared (NIR) dye IRDye 800CW (LI-COR Biosciences Inc.), as previously reported [24]. Despite the excellent tumor take rate of the THJ-16T cell line [20], baseline BLI was carried out to confirm the growth of THJ-16T^{Luc} tumors. To this end, D-luciferin (3 mg/mouse) was injected peritoneally to the nude mice and BLI was acquired with an IVIS Spectrum (Perkin Elmer Inc.) 10 min after injection. Tumor-bearing mice were divided into ICAM-1-targeted imaging group and blocking group (n = 3 for each group). Mice in the ICAM-1-targeted imaging group were injected with IRDye 800CW-ICAM-1 (100 μg/mouse). Whereas for the mice in the blocking group, 1 mg of unlabeled R6–5-D6 was given 24 h prior to injection of the IRDye 800CW-ICAM-1 (100 μg/mouse). Fluorescent imaging ($\lambda_{ex/em}$ 745/800 nm) was acquired 48 h after injection of the fluorescent tracer using the IVIS Spectrum. The data were analyzed using a Living Image 4.5.5 (IVIS Imaging Systems) software.

Biodistribution and histopathology studies

After termination of the immunoPET imaging studies, the mice were sacrificed and samples including blood were obtained and weighed. The radioactivity of the collected samples was counted using the automated γ-counter and the uptake of the radiotracers in different organs/tissues was calculated and given as %ID/g (mean ± SD). The detailed protocols and reagents used for immunofluorescent staining were available from the authors upon rational request.

Statistical analysis

Statistical analysis was performed using GraphPad and Microsoft Excel. All data are presented as the mean value ± SD. Group data were compared using the two-tailed Student t test, and multiple comparisons of grouped data were calculated using two-way ANOVA. $p < 0.05$ was considered statistically significant.

Results

^{64}Cu-NOTA-ICAM-1 immunoPET imaging of melanomas

As a continuation of our previous work [19, 25], this study intended to explore novel biomarkers for melanomas. Flow cytometry assessment showed that both the two tested melanoma cell lines (i.e., A375 and SK-MEL-5) were ICAM-1-positive (Fig. 1). ^{64}Cu-NOTA-ICAM-1 was developed with a high radiolabeling yield (> 70%) and an excellent RCP (> 99%) as tested by radio-TLC. The specific activity of the ^{64}Cu-labeled antibody was estimated to be in the range of 3.5–7 mCi/nmol. ^{64}Cu-NOTA-ICAM-1 was highly stable within 48 h and minimal ^{64}Cu was released from the radiotracer (Supplementary Fig. 1). ImmunoPET imaging with ^{64}Cu-NOTA-ICAM-1 clearly visualized subcutaneous A375 xenografts at 24 h and 48 h post-injection of the radiotracer. In comparison, uptake in other major organs was quite low as seen from the given maximum intensity projection (MIP) images (Fig. 2a). Quantitative evaluation of the PET data showed a tumor uptake of 10.94 ± 3.22 %ID/g at 48 h post-injection of the radiotracer, whereas the corresponding uptake in the blood pool, liver, spleen, and kidney was 9.44 ± 5.43 %ID/g, 8.26 ± 0.81 %ID/g, 6.04 ± 1.14 %ID/g, and 4.48 ± 1.01 %ID/g, respectively ($n = 5$, Fig. 2b). Biodistribution study yielded fair agreement with the above region of interest (ROI) analysis results, demonstrating a higher radioactivity concentration in the tumors (21.28 ± 6.56 %ID/g, $n = 5$) but a comparable concentration in other major organs or tissues (Fig. 2c).

To showcase the specificity of ^{64}Cu-NOTA-ICAM-1, we radiolabeled the nonspecific human IgG with ^{64}Cu and the diagnostic value of the developed ^{64}Cu-NOTA-IgG was investigated in another group of A375-bearing melanoma models. Not surprisingly, ^{64}Cu-NOTA-IgG immunoPET imaging had no affirmative value in imaging ICAM-1-positive melanomas as the tumor signal was not distinct from the background signal (Fig. 2d–f). ^{64}Cu-NOTA-IgG mostly resided in the circulation at 48 h post-injection, with an uptake of 14.77 ± 5.58 %ID/g based on the ROI analysis and a comparative uptake of 17.82 ± 7.70 %ID/g as revealed by the ex vivo biodistribution data. When compared with ^{64}Cu-NOTA-ICAM-1, the accumulation of ^{64}Cu-NOTA-IgG was slightly higher in the livers and kidneys, two organs where antibodies were degraded or excreted after lengthy circulation.

Immunofluorescent staining and imaging of the excised A375 tumor demonstrated a predominant membrane expression of ICAM-1 protein in A375 cells (Fig. 2g). Taken together, ICAM-1 is a promising diagnostic marker for melanomas. ImmunoPET imaging with ^{64}Cu-NOTA-ICAM-1 could readily map ICAM-1 expression and stratify ICAM-1-positive melanomas.

^{64}Cu-NOTA-ICAM-1 immunoPET imaging of ATCs

Currently, AIC100, an ICAM-1-targeted CAR-T therapy developed by AffyImmune Therapeutics, is undergoing a phase I clinical trial for radioiodine-refractory thyroid cancers including the ATC. Therefore, we further examined the ability of ^{64}Cu-NOTA-ICAM-1 immunoPET in imaging advanced thyroid cancers. Flow cytometry screening showed that four of the five included thyroid cancer cell lines were ICAM-1-positive (Fig. 3a). ImmunoPET imaging showed unique distribution patterns of ^{64}Cu-NOTA-ICAM-1 in ATC-bearing R2G2 mice. That is, despite the abundant tumor uptake, ^{64}Cu-NOTA-ICAM-1 was rapidly captured by the spleens (Fig. 3b). Based on the ROI analysis (Fig. 3c), tumor uptake at the initial time-point was 7.73 ± 1.38 %ID/g and the uptake value increased in a time-dependent manner. However, there was no statistical difference between the uptake at the last two time-points (15.03 ± 0.51 %ID/g at 24 h vs. 16.47 ± 1.21 %ID/g at 48 h, $p = 0.34$). ROI analysis revealed a peak spleen uptake of 14.00 ± 2.11 %ID/g at 4 h after administration of the radiotracer, which gradually decreased over the imaging period (12.90 ± 1.15 %ID/g at 12 h, 12.80 ± 0.27 %ID/g at 24 h, and 11.20 ± 0.44 %ID/g at 48 h; $n = 3$). Biodistribution study showed an average tumor uptake of 26.30 ± 0.76 %ID/g and a spleen uptake of 21.84 ± 5.20 %ID/g ($n = 3$), with uptake in other organs/tissues less than 10 %ID/g (Fig. 3d). These results not only demonstrated the potency of ^{64}Cu-NOTA-ICAM-1 immunoPET in diagnosing ATCs in an ICAM-1-dependent manner but also provided the first evidence that ^{64}Cu-NOTA-ICAM-1 was rapidly captured by the spleen of the ultra-immunodeficient R2G2 mice.

^{64}Cu-NOTA-IgG immunoPET imaging of ATCs

We also performed ^{64}Cu-NOTA-IgG immunoPET imaging in ATC-bearing R2G2 mice. MIP and coronal immunoPET images showed that tumor uptake of ^{64}Cu-NOTA-IgG was slightly higher than uptake by surrounding tissues (Fig. 4a, b). Due to the absence of active targeting, ^{64}Cu-NOTA-IgG circulated significantly longer than ^{64}Cu-NOTA-ICAM-1, as verified by the blood pool concentration at 48 h on ROI analysis (11.40 ± 1.57 %ID/g vs. 6.80 ± 1.31 %ID/g, $p = 0.02$; Fig. 4c). Different circulation time of the two radiotracers was further validated by the biodistribution study, where blood accumulation of ^{64}Cu-NOTA-IgG was statistically higher than that of ^{64}Cu-NOTA-ICAM-1 (16.21 ± 2.73 %ID/g vs. 8.62 ± 2.35 %ID/g, $p = 0.02$; Fig. 4d). As shown by the biodistribution data, spleen uptake of ^{64}Cu-NOTA-IgG was higher in ATC-bearing R2G2 mice than in the A375-bearing nude mice (12.34 ± 2.53 %ID/g vs. 4.89 ±0.63 %ID/g, $p = 0.046$). In ATC-bearing R2G2 mice, analysis of the biodistribution data showed that tumor uptake of ^{64}Cu-NOTA-ICAM-1 was substantially higher than that of ^{64}Cu-NOTA-IgG (26.30 ± 0.76 %ID/g vs. 12.67 ± 2.68 %ID/g, $p = 0.001$). Immunofluorescent staining of the fixed ATC tumor section also showed a predominant membrane expression of ICAM-1 (Fig. 4e). These results supported our hypothesis that immunoPET imaging with ^{64}Cu-NOTA-ICAM-1, but not with ^{64}Cu-NOTA-

IgG, could serve as a scouting tool to detect subcutaneous ATCs in a marker-dependent manner.

^{64}Cu-NOTA-ICAM-1 immunoPET imaging of orthotopic ATCs

To test the diagnostic efficacy of ^{64}Cu-NOTA-ICAM-1 in orthotopic thyroid cancer models, we carried out immunoPET imaging in orthotopic ATC-bearing R2G2 mice. Similar to that observed in the subcutaneous ATC models, ^{64}Cu-NOTA-ICAM-1 immunoPET/CT imaging detected orthotopic ATCs with high clarity and contrast (Fig. 5a–c). Quantitative analysis showed that tumor uptake at 4 h, 12 h, 24 h, and 48 h was 7.45 ± 1.42 %ID/g, 14.00 ± 1.88 %ID/g, 15.42 ± 1.53 %ID/g, and 13.20 ± 0.81 %ID/g ($n = 4$), respectively (Fig. 5d). But multiple comparisons showed no statistical differences of the tumor uptake at the last three time-points. In comparison with the spleen uptake of ^{64}Cu-NOTA-ICAM-1 in subcutaneous ATC models (Fig. 3d), we found even higher spleen uptake of ^{64}Cu-NOTA-ICAM-1 in the orthotopic ATC models (21.84 ± 5.20 %ID/g vs. 39.30 ± 4.98 %ID/g, $p = 0.0137$; Fig. 5e). Orthotopic ATC models suffer from severe tumor burden and the average volume of the spleens was smaller than that of the subcutaneous ATC models, which consequently contributed to the higher spleen uptake of the radiotracer in terms of %ID/g. Similarly, a mass of ICAM-1 expression was found on the plasmalemma of THJ-16T cells inoculated in the left thyroid gland of the R2G2 mice (Fig. 5f). These results indicated the potency of ^{64}Cu-NOTA-ICAM-1 immunoPET in delineating not only the subcutaneous but also the orthotopic ATCs.

Bioluminescent and fluorescent imaging of orthotopic ATCs

To further validate the specificity of R6–5-D6-based ICAM-1-targeted imaging, we developed a NIR fluorescent imaging probe IRDye 800CW-ICAM-1 using the mAb R6–5-D6. The tumor-targeting specificity of this probe was tested in orthotopic ATC models, which were established using the THJ-16T^{Luc} cell line and nude mice. One month after tumor cell inoculation, BLI showed localized signal in thyroid areas, indicating the successful establishment of the tumor models (Fig. 6a). Fluorescent imaging of the same mice demonstrated intense signal in the thyroid areas and also in the livers (Fig. 6b), indicating the tumor-targeting capacity and hepatobiliary clearance of IRDye 800CW-ICAM-1. BLI of mice pre-injected with cold R6–5-D6 (1 mg/mouse) also suggested the growth of the tumors (Fig. 6c). However, fluorescent imaging of the mice failed to clearly delineate the tumors (Fig. 6d), presumably because R6–5-D6 saturated ICAM-1 on tumor cells and relocated the fluorescent probe to the livers. The average bioluminescent intensity in the ICAM-1-targeted imaging group and in the blocking group was 406.3 ± 200.4 ($n = 3$) and 375.3 ± 17.75 ($n = 3$), respectively. There was no statistical difference in the tumor burden in the two groups ($p = 0.8850$). However, fluorescent signal in the ICAM-1-targeted imaging group was substantially higher than that in the blocking group in terms of tumor-to-liver ratio (1.434 ± 0.2367 [$n = 3$] vs. 0.3097 ± 0.04401 [$n = 3$], $p = 0.0095$). The data were in concert with the above immunoPET imaging results and further demonstrated the targeting specificity of R6–5-D6-derived imaging tracers.

Cold IgG extended the circulation of ^{64}Cu-NOTA-ICAM-1

Previous studies have elucidated a pivotal role of Fc/Fc-gamma receptor (FcγR) interaction in manipulating the in vivo fate of antibody therapeutics, especially in ultra-immunodeficient mice like NSG and NOD/SCID [26]. To the best of our knowledge, our study is the first report using the R2G2 mice to establish both subcutaneous and orthotopic tumor models. We also found the tricky circulation of the murine antibody-derived immunoPET probe (i.e., ^{64}Cu-NOTA-ICAM-1) in R2G2 mice. We tested whether pre-dosing with the unlabeled human IgG could partially saturate the FcγR in the spleen, thereby prolonging the circulation of ^{64}Cu-NOTA-ICAM-1 and concomitantly reducing spleen deposition. When comparing uptake profiles to that of the non-blocking group (Fig. 3b–d), preloading with 1.5 mg of human IgG per mouse one day before injection of ^{64}Cu-NOTA-ICAM-1 visually extended the circulation of ^{64}Cu-NOTA-ICAM-1 (Supplementary Fig. 2a, b). But the increase extent was not statistically significant, supported by the blood accumulation on ROI analysis (11.85 ± 3.18 %ID/g vs. 6.80 ± 1.31 %ID/g, $p = 0.08$; Supplementary Fig. 2c) and on biodistribution analysis (15.05 ± 4.20 %ID/g vs. 8.62 ± 2.35 %ID/g, $p = 0.11$; Supplementary Fig. 2d). After analyzing the biodistribution data, we found IgG blocking also failed to reduce spleen deposition of the radiotracer (21.13 ± 6.32 %ID/g vs. 21.84 ± 5.20 %ID/g, $p = 0.11$), but it did not compromise tumor uptake (24.09 ± 7.40 %ID/g vs. 26.30 ± 0.76 %ID/g, $p = 0.11$). It remains to be determined if murine antibodies (e.g., the parental antibody R6–5-D6) can block the high spleen uptake of the reported radiotracer.

Discussion

A variety of molecular targets predominantly expressed on tumor cells have been exploited to develop immunoPET probes. Of them, receptor tyrosine kinases (e.g., epidermal growth factor receptors family receptors) have been thoroughly investigated and several immunoPET probes have been successfully translated and used in a clinical scenario [15, 27]. For instance, the clinical application of two human epidermal growth factor receptor-2 specific immunoPET probes, ^{89}Zr-trastuzumab and ^{89}Zr-pertuzumab [13, 14], is fundamentally improving the clinical management of patients with breast cancer. These two immunoPET imaging approaches evaluated HER2 status in heterogeneous tumor lesions and delineated brain metastases, which sometimes might be equivocal on ^{18}F-FDG PET images [28]. In the translation of immunoPET probes, one concern is the radiation exposures generated by the probes, especially for the liver and kidney [29]. Strategies like improvement of the PET/CT equipment, reduction of the administered activity, and proper blocking study using cold antibodies may lower radiation doses to patients and health care staff. In the case of ^{64}Cu-NOTA-ICAM-1 immunoPET, we found that ICAM-1 uptake was low in normal organs except that in the spleens of the R2G2 mice, which was caused, in part, by the property of the mouse strain (as discussed below). Looking forward, continuous renovation of ICAM-1-directed immunoPET may further improve the image quality while lowering radiation exposure to the normal organs or tissues.

In light of the helpful information provided by immunoPET, we think that ICAM-1-targeted immunoPET is useful to visualize the varying levels of ICAM-1 in different tumor types [3]. Moreover, immunoPET imaging enables direct assessment of target occupancy and plasma

concentration of the antibody drugs [15, 30, 31]. Therefore, incorporation of ICAM-1-specific immunoPET may accelerate the development of ICAM-1-directed therapeutics [32]. In addition to its use in cancer management, ^{64}Cu-NOTA-ICAM-1 immunoPET may also detect acute renal failure and autoimmune diseases because ICAM-1 is preferentially expressed under these two conditions [33, 34]. Substantial studies have reported that ICAM-1 is involved in the clustering of T cells and the therapeutic efficacy of anti-CTLA-4 therapy [35, 36]. Therefore, it is interesting to investigate if ICAM-1-targeted immunoPET can help understand the complex aggregation of T cells in immunocompetent mouse models.

Both the immunodeficiency status of the mouse strains and the properties of the antibodies affect the in vivo fate of antibody-based therapeutics and diagnostic probes [26, 37, 38]. In such a setting, we used two mouse strains with different immunodeficiency status to investigate the in vivo performance of ^{64}Cu-NOTA-ICAM-1. Our results showed that the circulation of the mouse IgG2a-derived probe (i.e., ^{64}Cu-NOTA-ICAM-1) was inversely correlated with the immunodeficiency degree of the mouse strains. Together with the results reported by Sharma et al. [26], we may conclude that the circulation of humanized IgG1- and mouse IgG2a-based diagnostic or therapeutic agents is heavily affected by the mouse strains. However, highly immunodeficient mouse strains are widely used for establishing patient-derived xenografts (PDX) and for reproducibly recapitulating distant metastatic tumor models. There are several strategies to enhance the tumor uptake of immunoPET probes while reducing spleen capture of the probes. One such approach is to block the Fc/FcγR interaction between antibodies and FcγR-expressing cells, which can be realized by using deglycosylated antibodies or FcγR-blocking agents [26, 37, 39–41]. In our hands, preloading with the human IgG slightly prolonged the retention of ^{64}Cu-NOTA-ICAM-1 in the circulation, but the increase was not statistically significant. Other alternative approaches may be adapted to improve the imaging quality in future studies. It is worthwhile to mention that the treatment outcome of certain therapeutic antibodies, such as anti-CTLA-4 and anti-PD-L1 antibodies, is reported to be FcγR-dependent [42–44]. Therefore, additional attention should be paid in the antibody engineering when an anti-ICAM-1 antibody is used for both immunoPET imaging and cancer therapy.

Despite the promising results of the antibody-based ^{64}Cu-NOTA-ICAM-1 immunoPET imaging and potential strategies to improve the imaging quality, radionuclides (e.g., ^{64}Cu, ^{89}Zr, and ^{124}I) of long half-lives are needed to match the lengthy circulation of mAbs. Due to their smaller size (15 KDa) and high affinity, Nanobodies have emerged as "magic bullets" for molecular imaging in recent years [45]. Moreover, radionuclides (e.g., ^{68}Ga, ^{99m}Tc, and ^{18}F) of short half-lives are well suited to the radiolabeling of Nanobodies [46, 47]. We have produced alpaca-derived Nanobodies targeting human ICAM-1 and our ongoing studies are interrogating the theranostic value of radiotracers/radioligands based on these smaller antibody vectors. We believe that these upcoming results will help us more thoroughly understand the theranostic value of ICAM-1 in more broad human malignancies.

Conclusion

In summary, our results demonstrate that ICAM-1 is a promising biomarker for melanomas and ATCs. ^{64}Cu-NOTA-ICAM-1 immunoPET is a promising technique to image ICAM-1 expression in these two types of solid tumors.

Supplementary Material

Refer to Web version on PubMed Central for supplementary material.

Acknowledgments

References

1. Reina M, Espel E. Role of LFA-1 and ICAM-1 in cancer. Cancers (Basel). 2017;9 10.3390/cancers9110153.

2. Yang L, Froio RM, Sciuto TE, Dvorak AM, Alon R, Luscinskas FW. ICAM-1 regulates neutrophil adhesion and transcellular migration of TNF-alpha-activated vascular endothelium under flow. Blood. 2005;106:584–92. 10.1182/blood-2004-12-4942. [PubMed: 15811956]

3. Hayes SH, Seigel GM. Immunoreactivity of ICAM-1 in human tumors, metastases and normal tissues. Int J Clin Exp Pathol. 2009;2:553–60. [PubMed: 19636402]

4. Hamai A, Meslin F, Benlalam H, Jalil A, Mehrpour M, Faure F, et al. ICAM-1 has a critical role in the regulation of metastatic melanoma tumor susceptibility to CTL lysis by interfering with PI3K/AKT pathway. Cancer Res. 2008;68:9854–64. 10.1158/0008-5472.CAN-08-0719. [PubMed: 19047166]

5. Zhang P, Goodrich C, Fu C, Dong C. Melanoma upregulates ICAM-1 expression on endothelial cells through engagement of tumor CD44 with endothelial E-selectin and activation of a PKCalpha-p38-SP-1 pathway. FASEB J. 2014;28:4591–609. 10.1096/fj.11-202747. [PubMed: 25138157]

6. Galore-Haskel G, Baruch EN, Berg AL, Barshack I, Zilinsky I, Avivi C, et al. Histopathological expression analysis of intercellular adhesion molecule 1 (ICAM-1) along development and progression of human melanoma. Oncotarget. 2017;8:99580–6. 10.18632/oncotarget.20884. [PubMed: 29245925]

7. Buitrago D, Keutgen XM, Crowley M, Filicori F, Aldailami H, Hoda R, et al. Intercellular adhesion molecule-1 (ICAM-1) is up-regulated in aggressive papillary thyroid carcinoma. Ann Surg Oncol. 2012;19:973–80. 10.1245/s10434-011-2029-0. [PubMed: 21879273]

8. Min IM, Shevlin E, Vedvyas Y, Zaman M, Wyrwas B, Scognamiglio T, et al. CAR T therapy targeting ICAM-1 eliminates advanced human thyroid tumors. Clin Cancer Res. 2017;23:7569–83. 10.1158/1078-0432.CCR-17-2008. [PubMed: 29025766]

9. Vedvyas Y, McCloskey JE, Yang Y, Min IM, Fahey TJ, Zarnegar R, et al. Manufacturing and preclinical validation of CAR T cells targeting ICAM-1 for advanced thyroid cancer therapy. Sci Rep. 2019;9:10634 10.1038/s41598-019-46938-7. [PubMed: 31337787]

10. James ML, Gambhir SS. A molecular imaging primer: modalities, imaging agents, and applications. Physiol Rev. 2012;92:897–965. 10.1152/physrev.00049.2010. [PubMed: 22535898]

11. Guo P, Huang J, Wang L, Jia D, Yang J, Dillon DA, et al. ICAM-1 as a molecular target for triple negative breast cancer. Proc Natl Acad Sci U S A. 2014;111:14710–5. 10.1073/pnas.1408556111. [PubMed: 25267626]

12. Bensch F, Smeenk MM, van Es SC, de Jong JR, Schroder CP, Oosting SF, et al. Comparative biodistribution analysis across four different (89)Zr-monoclonal antibody tracers-the first step

towards an imaging warehouse. Theranostics. 2018;8:4295–304. 10.7150/thno.26370. [PubMed: 30214621]

13. Bensch F, Brouwers AH, Lub-de Hooge MN, de Jong JR, van der Vegt B, Sleijfer S, et al. (89)Zr-trastuzumab PET supports clinical decision making in breast cancer patients, when HER2 status cannot be determined by standard work up. Eur J Nucl Med Mol Imaging. 2018;45:2300–6. 10.1007/s00259-018-4099-8. [PubMed: 30058029]

14. Ulaner GA, Lyashchenko SK, Riedl C, Ruan S, Zanzonico PB, Lake D, et al. First-in-human human epidermal growth factor receptor 2-targeted imaging using (89)Zr-Pertuzumab PET/CT: dosimetry and clinical application in patients with breast cancer. J Nucl Med. 2018;59:900–6. 10.2967/jnumed.117.202010. [PubMed: 29146695]

15. Wei W, Ni D, Ehlerding EB, Luo Q-Y, Cai W. PET imaging of receptor tyrosine kinases in cancer. Mol Cancer Ther. 2018;17: 1625–36. 10.1158/1535-7163.mct-18-0087. [PubMed: 30068751]

16. Lamberts LE, Menke-van der Houven van Oordt CW, ter Weele EJ, Bensch F, Smeenk MM, Voortman J, et al. ImmunoPET with anti-mesothelin antibody in patients with pancreatic and ovarian cancer before anti-mesothelin antibody-drug conjugate treatment. Clin Cancer Res. 2016;22:1642–52. 10.1158/1078-0432.CCR-15-1272. [PubMed: 26589435]

17. Wei W, Jiang D, Ehlerding EB, Luo Q, Cai W. Noninvasive PET imaging of T cells. Trends Cancer. 2018;4:359–73. 10.1016/j.trecan.2018.03.009. [PubMed: 29709260]

18. Cai W, Rao J, Gambhir SS, Chen X. How molecular imaging is speeding up antiangiogenic drug development. Mol Cancer Ther. 2006;5:2624–33. 10.1158/1535-7163.MCT-06-0395. [PubMed: 17121909]

19. Wei W, Jiang D, Ehlerding EB, Barnhart TE, Yang Y, Engle JW, et al. CD146-targeted multimodal image-guided photoimmunotherapy of melanoma. Adv Sci (Weinh). 2019;6:1801237 10.1002/advs.201801237. [PubMed: 31065511]

20. Wei W, Jiang D, Rosenkrans ZT, Barnhart TE, Engle JW, Luo Q, et al. HER2-targeted multimodal imaging of anaplastic thyroid cancer. Am J Cancer Res. 2019;9:2413–27. [PubMed: 31815043]

21. Nucera C, Nehs MA, Mekel M, Zhang X, Hodin R, Lawler J, et al. A novel orthotopic mouse model of human anaplastic thyroid carcinoma. Thyroid. 2009;19:1077–84. 10.1089/thy.2009.0055. [PubMed: 19772429]

22. Jin Y, Liu M, Sa R, Fu H, Cheng L, Chen L. Mouse models of thyroid cancer: bridging pathogenesis and novel therapeutics. Cancer Lett. 2020;469:35–53. 10.1016/j.canlet.2019.09.017. [PubMed: 31589905]

23. Yang Y, Hernandez R, Rao J, Yin L, Qu Y, Wu J, et al. Targeting CD146 with a 64Cu-labeled antibody enables in vivo immunoPET imaging of high-grade gliomas. Proc Natl Acad Sci U S A. 2015;112:E6525–34. 10.1073/pnas.1502648112. [PubMed: 26553993]

24. Cohen R, Vugts DJ, Stigter-van Walsum M, Visser GW, van Dongen GA. Inert coupling of IRDye800CW and zirconium-89 to monoclonal antibodies for single- or dual-mode fluorescence and PET imaging. Nat Protoc. 2013;8:1010–8. 10.1038/nprot.2013.054. [PubMed: 23619892]

25. Wei W, Ehlerding EB, Lan X, Luo Q, Cai W. PET and SPECT imaging of melanoma: the state of the art. Eur J Nucl Med Mol Imaging. 2018;45:132–50. 10.1007/s00259-017-3839-5. [PubMed: 29085965]

26. Sharma SK, Chow A, Monette S, Vivier D, Pourat J, Edwards KJ, et al. Fc-mediated anomalous biodistribution of therapeutic antibodies in immunodeficient mouse models. Cancer Res. 2018;78: 1820–32. 10.1158/0008-5472.Can-17-1958. [PubMed: 29363548]

27. Pereira PMR, Abma L, Henry KE, Lewis JS. Imaging of human epidermal growth factor receptors for patient selection and response monitoring - from PET imaging and beyond. Cancer Lett. 2018;419:139–51. 10.1016/j.canlet.2018.01.052. [PubMed: 29414302]

28. Lin NU, Bellon JR, Winer EP. CNS metastases in breast cancer. J Clin Oncol. 2004;22:3608–17. 10.1200/JCO.2004.01.175. [PubMed: 15337811]

29. Pandit-Taskar N, O'Donoghue JA, Beylergil V, Lyashchenko S, Ruan S, Solomon SB, et al. (8)(9)Zr-huJ591 immuno-PET imaging in patients with advanced metastatic prostate cancer. Eur J Nucl Med Mol Imaging. 2014;41:2093–105. 10.1007/s00259-014-2830-7. [PubMed: 25143071]

30. Moek KL, Giesen D, Kok IC, de Groot DJA, Jalving M, Fehrmann RSN, et al. Theranostics using antibodies and antibody-related therapeutics. J Nucl Med. 2017;58:83S–90S. 10.2967/jnumed.116.186940. [PubMed: 28864618]

31. Burvenich IJG, Parakh S, Parslow AC, Lee ST, Gan HK, Scott AM. Receptor occupancy imaging studies in oncology drug development. AAPS J. 2018;20:43 10.1208/s12248-018-0203-z. [PubMed: 29520671]

32. Lamberts LE, Williams SP, Terwisscha van Scheltinga AG, Lub-de Hooge MN, Schroder CP, Gietema JA, et al. Antibody positron emission tomography imaging in anticancer drug development. J Clin Oncol. 2015;33:1491–504. 10.1200/JCO.2014.57.8278. [PubMed: 25779566]

33. Wu X, Guo R, Wang Y, Cunningham PN. The role of ICAM-1 in endotoxin-induced acute renal failure. Am J Physiol Renal Physiol. 2007;293:F1262–71. 10.1152/ajprenal.00445.2006. [PubMed: 17670897]

34. Mar D, Gharib SA, Zager RA, Johnson A, Denisenko O, Bomsztyk K. Heterogeneity of epigenetic changes at ischemia/reperfusion- and endotoxin-induced acute kidney injury genes. Kidney Int. 2015;88:734–44. 10.1038/ki.2015.164. [PubMed: 26061546]

35. Zumwalde NA, Domae E, Mescher MF, Shimizu Y. ICAM-1-dependent homotypic aggregates regulate CD8 T cell effector function and differentiation during T cell activation. J Immunol. 2013;191:3681–93. 10.4049/jimmunol.1201954. [PubMed: 23997225]

36. Hailemichael Y, Woods A, Fu T, He Q, Nielsen MC, Hasan F, et al. Cancer vaccine formulation dictates synergy with CTLA-4 and PD-L1 checkpoint blockade therapy. J Clin Invest. 2018;128:1338–54. 10.1172/JCI93303. [PubMed: 29480817]

37. Bournazos S, Wang TT, Dahan R, Maamary J, Ravetch JV. Signaling by antibodies: recent progress. Annu Rev Immunol. 2017;35:285–311. 10.1146/annurev-immunol-051116-052433. [PubMed: 28446061]

38. Warnders FJ, Lub-de Hooge MN, de Vries EGE, Kosterink JGW. Influence of protein properties and protein modification on biodistribution and tumor uptake of anticancer antibodies, antibody derivatives, and non-Ig scaffolds. Med Res Rev. 2018;38:1837–73. 10.1002/med.21498. [PubMed: 29635825]

39. Dalziel M, Crispin M, Scanlan CN, Zitzmann N, Dwek RA. Emerging principles for the therapeutic exploitation of glycosylation. Science. 2014;343:1235681 10.1126/science.1235681. [PubMed: 24385630]

40. Pincetic A, Bournazos S, DiLillo DJ, Maamary J, Wang TT, Dahan R, et al. Type I and type II Fc receptors regulate innate and adaptive immunity. Nat Immunol. 2014;15:707–16. 10.1038/ni.2939. [PubMed: 25045879]

41. Arlauckas SP, Garris CS, Kohler RH, Kitaoka M, Cuccarese MF, Yang KS, et al. In vivo imaging reveals a tumor-associated macrophage-mediated resistance pathway in anti-PD-1 therapy. Sci Transl Med. 2017;9 10.1126/scitranslmed.aal3604.

42. Ingram JR, Blomberg OS, Rashidian M, Ali L, Garforth S, Fedorov E, et al. Anti-CTLA-4 therapy requires an Fc domain for efficacy. Proc Natl Acad Sci U S A. 2018;115:3912–7. 10.1073/pnas.1801524115. [PubMed: 29581255]

43. Arce Vargas F, Furness AJS, Litchfield K, Joshi K, Rosenthal R, Ghorani E, et al. Fc effector function contributes to the activity of human anti-CTLA-4 antibodies. Cancer Cell. 2018;33:649–63 e4. 10.1016/j.ccell.2018.02.010. [PubMed: 29576375]

44. Dahan R, Sega E, Engelhardt J, Selby M, Korman AJ, Ravetch JV. FcgammaRs modulate the anti-tumor activity of antibodies targeting the PD-1/PD-L1 axis. Cancer Cell. 2015;28:285–95. 10.1016/j.ccell.2015.08.004. [PubMed: 26373277]

45. Chakravarty R, Goel S, Cai W. Nanobody: the "magic bullet" for molecular imaging? Theranostics. 2014;4:386–98. 10.7150/thno.8006. [PubMed: 24578722]

46. Keyaerts M, Xavier C, Heemskerk J, Devoogdt N, Everaert H, Ackaert C, et al. Phase I study of 68Ga-HER2-nanobody for PET/CT assessment of HER2 expression in breast carcinoma. J Nucl Med. 2016;57:27–33. 10.2967/jnumed.115.162024. [PubMed: 26449837]

47. Xing Y, Chand G, Liu C, Cook GJR, O'Doherty J, Zhao L, et al. Early phase I study of a (99m)Tc-labeled anti-programmed death ligand-1 (PD-L1) single-domain antibody in SPECT/CT

assessment of PD-L1 expression in non-small cell lung cancer. J Nucl Med. 2019;60:1213–20. 10.2967/jnumed.118.224170. [PubMed: 30796165]
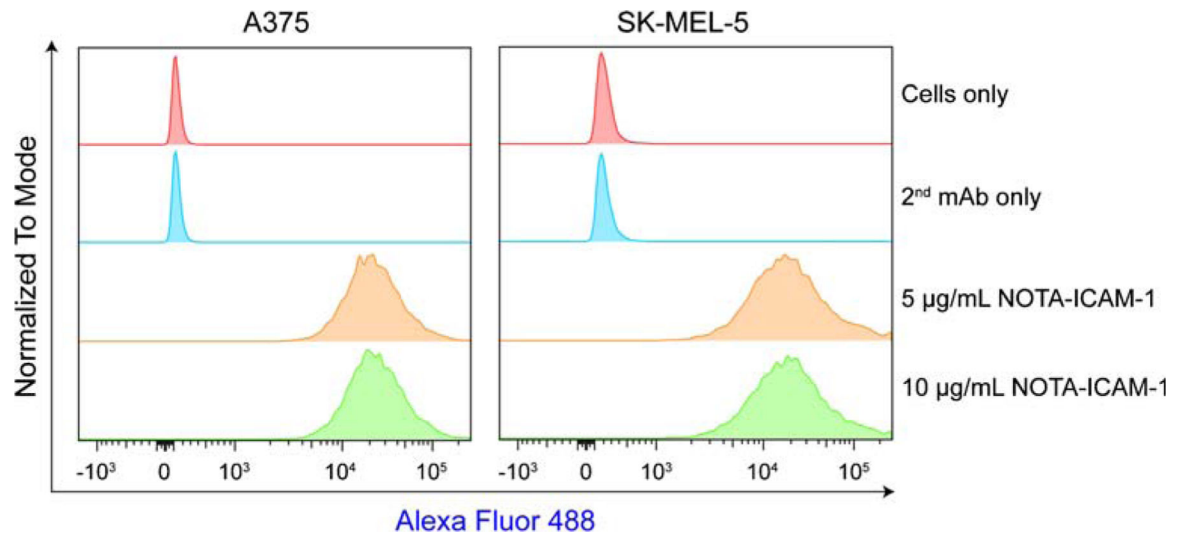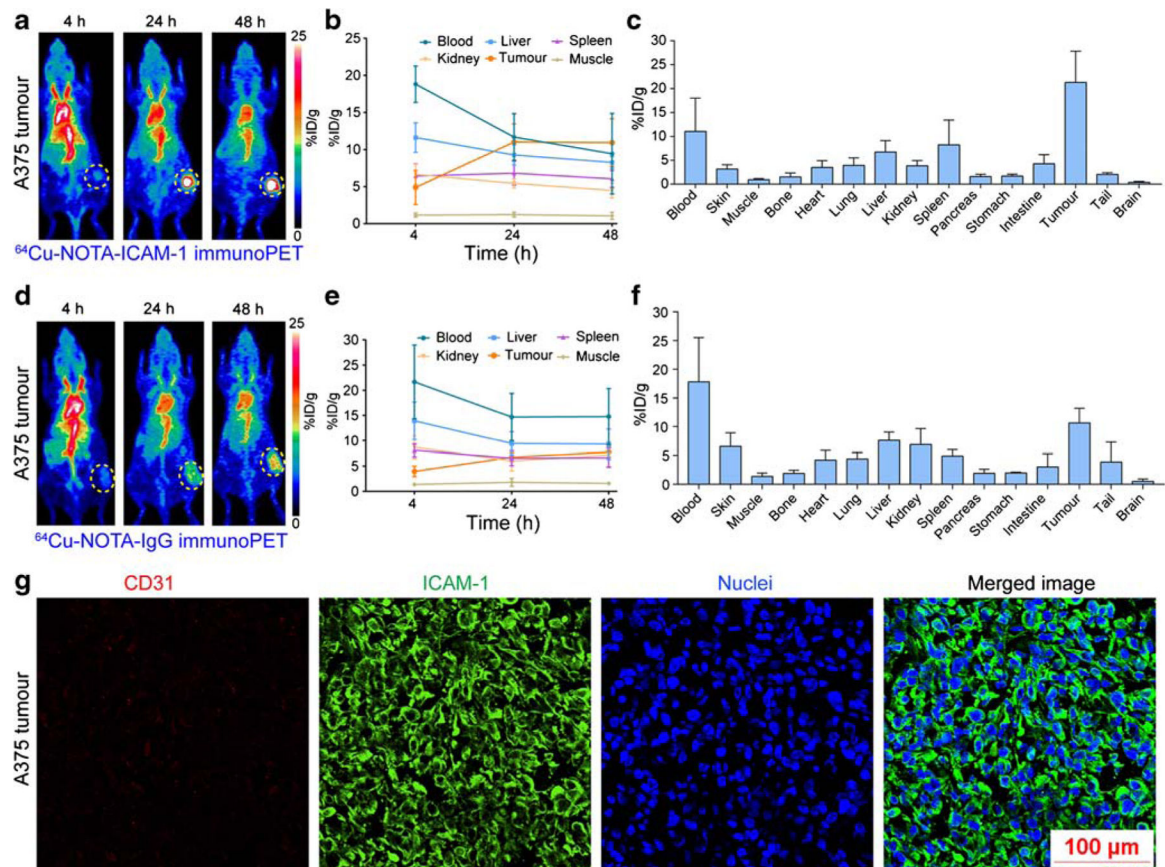
Fig. 1.
Flow cytometry assessment of ICAM-1 expression on melanoma cell lines

Fig. 2.

ImmunoPET imaging of ICAM-1-positive melanomas. **a** ^{64}Cu-NOTA-ICAM-1 immunoPET imaging of A375-bearing nude mice. Serial maximum intensity projection images of a representative mouse at different imaging time-points were given. **b** Region of interest analysis of ^{64}Cu-NOTA-ICAM-1 immunoPET imaging data. **c** Biodistribution study at 48 h post-injection of ^{64}Cu-NOTA-ICAM-1. **d** ^{64}Cu-NOTA-IgG immunoPET imaging of A375-bearing nude mice. Serial maximum intensity projection images of a representative mouse at different imaging time-points were given. **e** Region of interest analysis of ^{64}Cu-NOTA-IgG immunoPET imaging data. **f** Biodistribution study at 48 h post-injection of ^{64}Cu-NOTA-IGg. **g** Immunofluorescent imaging of a representative A375 tumor. The tumor section was stained for CD31 (red), ICAM-1 (green), and nuclei (blue). The tumors were indicated by yellow dotted circles
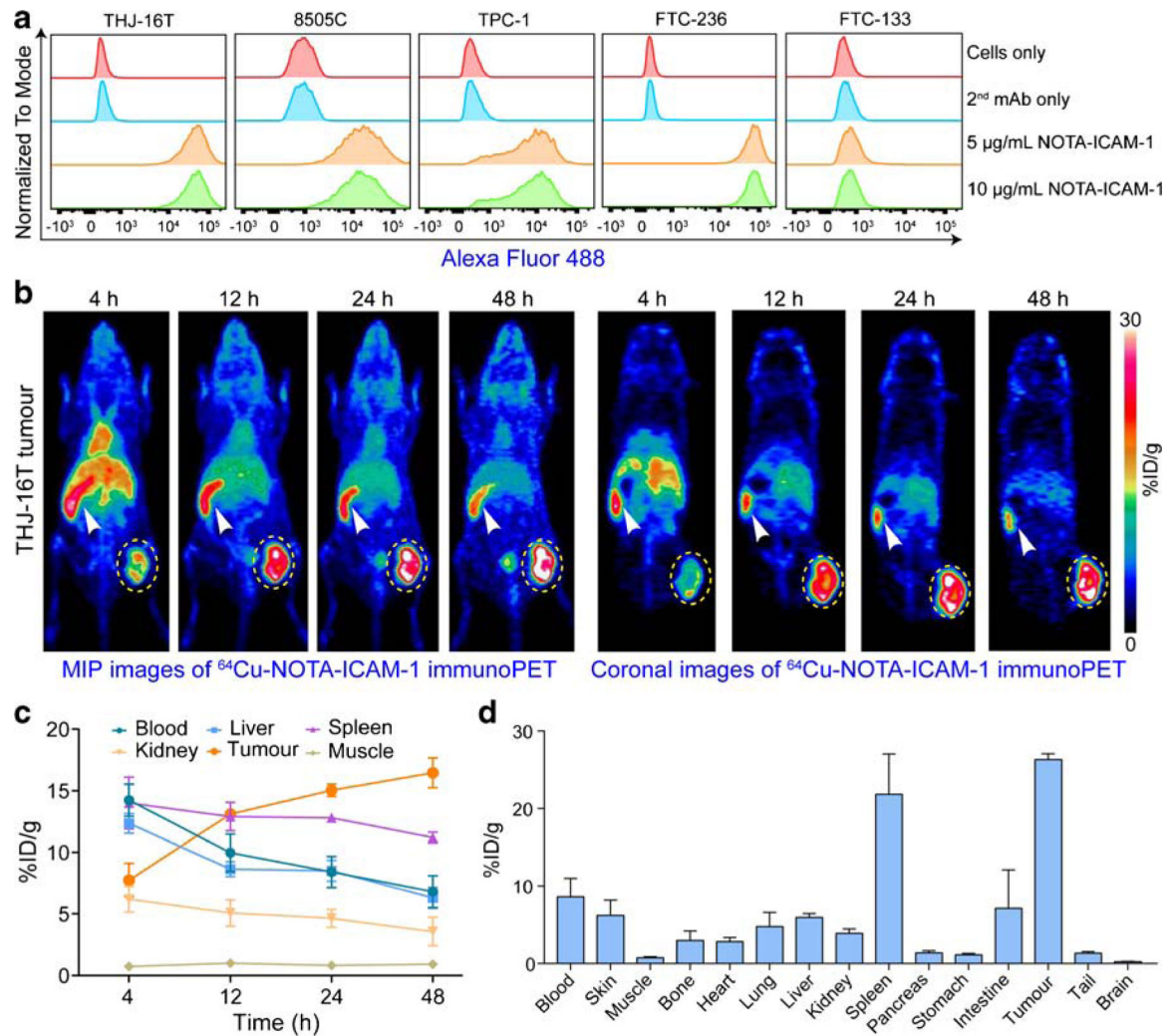
Fig. 3.

ImmunoPET imaging of ICAM-1 in subcutaneous anaplastic thyroid cancers. **a** Flow cytometry assessment of ICAM-1 expression on five thyroid cancer cell lines. **b** ^{64}Cu-NOTA-ICAM-1 immunoPET imaging of subcutaneous THJ-16T-bearing R2G2 mice. Maximum intensity projection (MIP) and coronal images of a representative mouse at different imaging time-points were given. **c** Region of interest analysis of ^{64}Cu-NOTA-ICAM-1 immunoPET imaging data. **d** Biodistribution study at 48 h post-injection of ^{64}Cu-NOTA-ICAM-1. The tumors were indicated by yellow dotted circles and spleens were indicated by white arrowheads
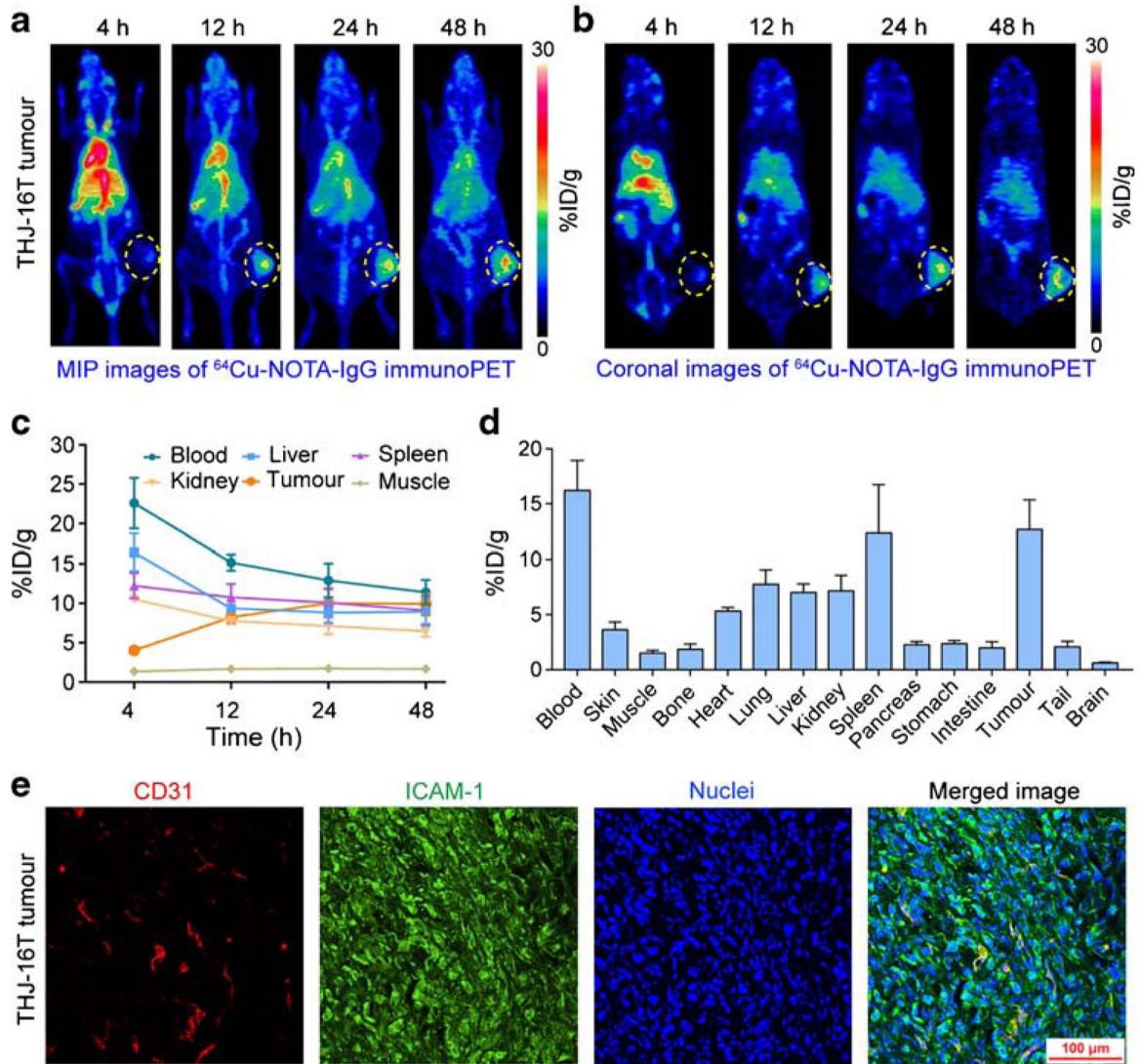
Fig. 4.
[64]Cu-NOTA-IgG immunoPET imaging of ICAM-1-positive subcutaneous anaplastic thyroid cancers. **a, b** ^{64}Cu-NOTA-IgG immunoPET imaging of subcutaneous THJ-16T-bearing R2G2 mice. Maximum intensity projection (MIP) and coronal images of a representative mouse at different imaging time-points were given. **c** Region of interest analysis of ^{64}Cu-NOTA-IgG immunoPET imaging data. **d** Biodistribution study at 48 h post-injection of ^{64}Cu-NOTA-IgG. **e** Immunofluorescent imaging of a subcutaneous THJ-16T tumor. The tumor section was stained for CD31 (red), ICAM-1 (green), and nuclei (blue). The tumors were indicated by yellow dotted circles
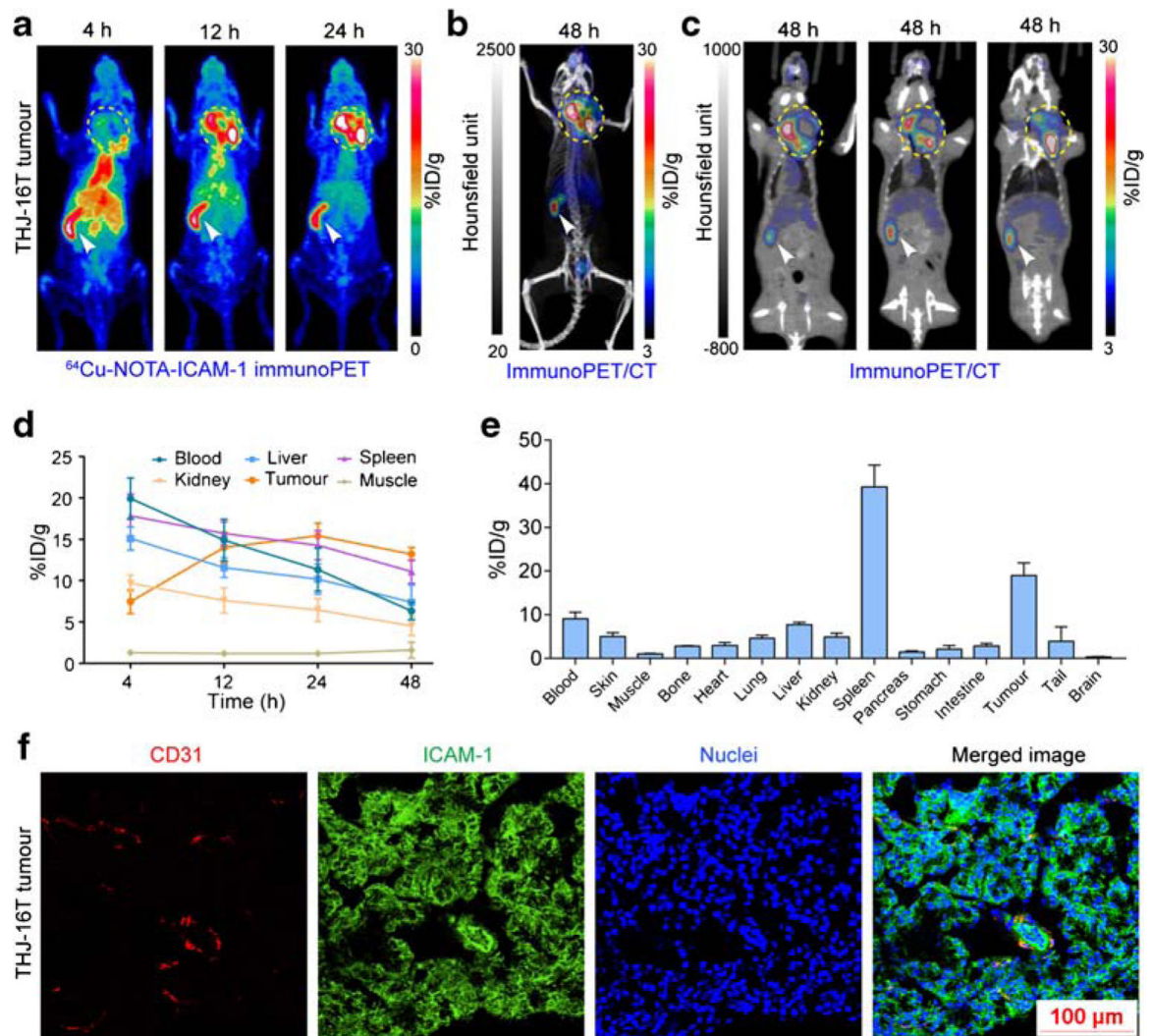
Fig. 5.

ImmunoPET and immunoPET/CT imaging of orthotopic anaplastic thyroid cancers. **a, b** ^{64}Cu-NOTA-ICAM-1 immunoPET and immunoPET/CT imaging of a representative orthotopic THJ-16T-bearing R2G2 mouse. **c** ImmunoPET/CT images at different slices of the same mouse showed expansion of the tumor into the surrounding tissues and necrosis inside the tumor. **d** Region of interest analysis of ^{64}Cu-NOTA-ICAM-1 immunoPET imaging data. **e** Biodistribution study at 48 h post-injection of ^{64}Cu-NOTA-ICAM-1. **f** Immunofluorescent imaging of a representative orthotopic THJ-16T tumor. The tumor section was stained for CD31 (red), ICAM-1 (green), and nuclei (blue). The tumors were indicated by yellow dotted circles and spleens were indicated by white arrowheads
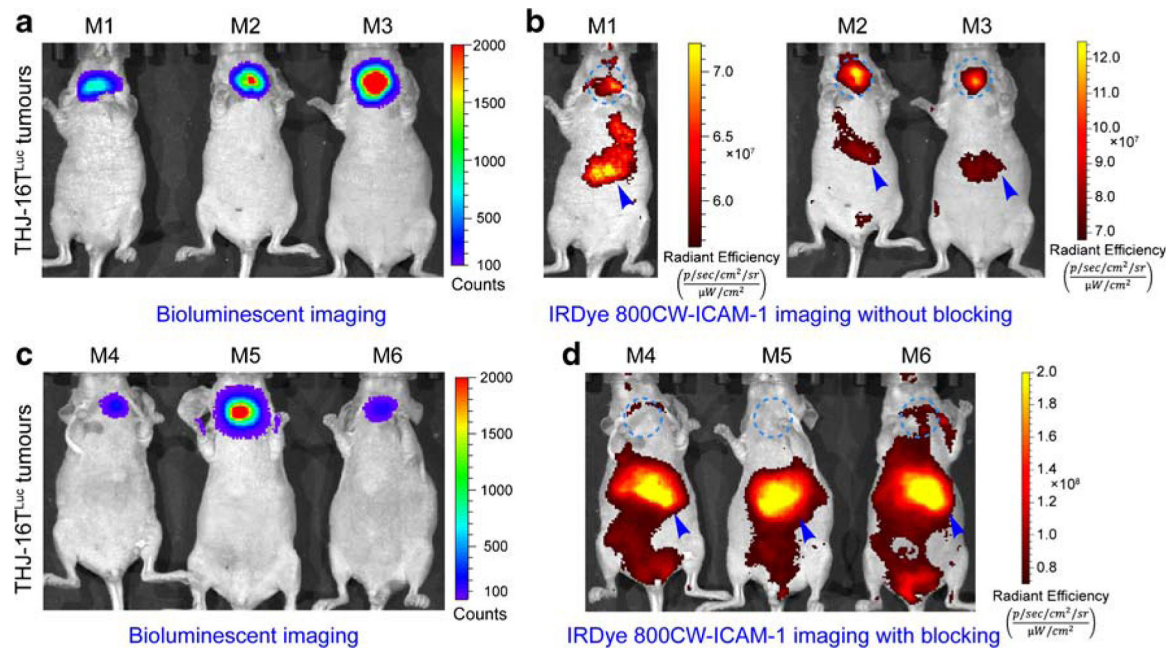
Fig. 6.
Bioluminescent imaging (BLI) and fluorescent imaging of orthotopic ATC models without or with R6–5-D6 blocking. **a** BLI of mice in the ICAM-1-targeted imaging group without R6–5-D6 blocking. The given image showed the growth of THJ-16T^Luc tumors. **b** Fluorescent imaging of the same mice 48 h after injection of IRDye 800CW-ICAM-1. The fluorescent tracer was eliminated from the hepatobiliary system with a proportion deposited in the orthotopic THJ-16T^Luc tumors. **c** BLI of mice in the blocking group showed comparable tumor burden. **d** Fluorescent imaging of the mice in the blocking group, which were injected first with a blocking dose of R6–5-D6 and then with the IRDye 800CW-ICAM-1. Fluorescent imaging acquired 48 h after injection of the tracer showed negligible signal in the thyroid areas, indicating saturation of the target by the blocking dose of R6–5-D6. The tumor areas were indicated by blue dotted circles and livers were indicated by blue arrowheads